Review of Scientific Instruments

Measurement of the lamella thickness during droplet impact onto differently wettable smooth surfaces using an extension of the LASER Pattern Shift Method with naturally occurring patterns

Cite as: Rev. Sci. Instrum. **92**, 105111 (2021); https://doi.org/10.1063/5.0060407
Submitted: 18 June 2021 • Accepted: 30 September 2021 • Published Online: 27 October 2021

P. Foltyn, L. K. Rihm, D. Ribeiro, et al.



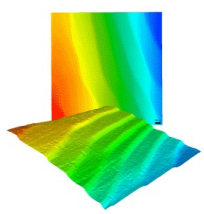
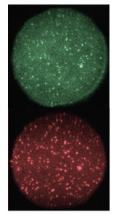

Review of Scientific Instruments ARTICLE scitation.org/journal/rsi

Measurement of the lamella thickness during droplet impact onto differently wettable smooth surfaces using an extension of the LASER Pattern Shift Method with naturally occurring patterns

Cite as: Rev. Sci. Instrum. 92, 105111 (2021); doi: 10.1063/5.0060407
Submitted: 18 June 2021 • Accepted: 30 September 2021 •
Published Online: 27 October 2021

P. Foltyn,[1,a] L. K. Rihm,[1,b] D. Ribeiro,[2,c] A. Silva,[2,d] and B. Weigand[1,e]

AFFILIATIONS

[1] Institute of Aerospace Thermodynamics, University of Stuttgart, Pfaffenwaldring 31, 70569 Stuttgart, Germany
[2] AEROG-LAETA, University of Beira Interior, Covilhã 6201-001, Portugal

[a] **Author to whom correspondence should be addressed:** patrick.foltyn@itlr.uni-stuttgart.de
[b] **Electronic mail:** lynn.rihm@web.de
[c] **Electronic mail:** daniela.santo.ribeiro@ubi.pt
[d] **Electronic mail:** andre@ubi.pt
[e] **Electronic mail:** bernhard.weigand@itlr.uni-stuttgart.de

ABSTRACT

This study shows that the LASER Pattern Shift Method (LPSM) is a powerful measurement technique for film thickness measurements. In this paper, the approach of the LPSM is extended, which is now able to measure the lamella thickness during droplet impacts on smooth surfaces using the naturally occurring air bubble shadows. With the help of this rather new measurement technique, the influence of different experimental parameters on the lamella thickness could be systematically assessed, e.g., the influence of impact velocity, liquid properties, and surface wettability. Upon comparing the obtained results to an analytical correlation in the literature, good agreement could be found for its validity range.

NOMENCLATURE

A and B	fitting parameters in the presented modification
a, b, c, γ, η, and τ_0	fitting parameters
D, D_{imp}, and D_{Spread}	diameter, impact diameter, and maximum spreading diameter (m)
d_S	distance between the bubble shadows (m)
d_{Cam}	LASER displacement detected using the camera (m)
h_F, $h_F(t)$, and $h_{\min}$	film/lamella thickness, time-dependent lamella thickness, and minimal lamella thickness (m)
$\widetilde{h}$	dimensionless film thickness $\tilde{h} = h_F\ /D_{imp}$ (-)
$\widetilde{h}_{inv}$	inviscid solution of the film thickness $\widetilde{h}_{inv} = \eta/(\tau+\tau_0)^2$ (-)
$\widetilde{h}_{res}$	dimensionless residual film thickness $\widetilde{h}_{res} = 0.79\mathrm{Re}^{-2/5}$ (-)
$\widetilde{h}_{visc}$	viscous solution of the film thickness $\widetilde{h}_{visc} = 4\gamma\sqrt{\tau}/(h\sqrt{Re})$ (-)
n and n_i	refractive index of i: F, fluid; P, prism; In, entrance medium; and Out, exit medium (-)
Re	Reynolds number $\mathrm{Re} = \rho\, Du/\mu$ (-)
S	falling height (m)
s_F	displacement of the LASER beam due to the liquid film (m)
t	time (s)
u and u_{imp}	velocity and impact velocity (m s^{-1})
We	Weber number $We = \rho\, Du^2/\sigma$ (-)
x	arbitrary variable
α and δ	angles of the LASER beam inside the prism and inside the liquid (°)

θ and θ_Y	apparent contact angle and Young contact angle (°)
μ	dynamic viscosity (Pa s)
ξ_t, ξ_{In}, and ξ_{Out}	angles of total reflection, incidence, and reflection (°)
ρ	density (kg m^{-3})
σ	surface tension (kg s^{-2})
τ	dimensionless time $\tau = ut/D$ (-)

I. INTRODUCTION

The impact of droplets onto smooth solid surfaces is a widespread research area due to its occurrence in many industrial processes. Examples include inkjet printers that specifically place individual ink droplets on the paper, surfaces that are cooled by using sprays, combustion processes where fuel is injected and hits the cylinder wall, or painting technology where surfaces are coated by sprays.[1] In all these processes, the impact of individual droplets onto a wall plays a major role. Here, the droplet can be described as a radially spreading lamella which is bounded by a bulging, almost circular rim.[2,3] This rim obscures the lateral view on the inner lamella and, therefore, the measurement of the lamella thickness.[4] During the droplet impact, even for walls at ambient temperature, a single bubble can be observed inside the liquid.[2] Its formation mechanism will be explained in detail. In this paper, this bubble is later used to determine the lamella thickness of the droplet during the impact process.

The first estimation of the lamella thickness was already proposed in 1995 by Yarin and Weiss[5] who derived analytically an inviscid solution for this problem. Years later, it could be observed numerically and experimentally that the minimal lamella thickness $h_{\min}$ at the maximum spreading diameter D_{Spread} (also called residual thickness) scales with the Reynolds number Re (Re $= \rho Du/\mu$) as $h_{\min} \sim D_{Spread}\mathrm{Re}^{-2/5}$.[6–10] Here, D and u are the droplet diameter and the impact velocity and ρ and μ are the liquid density and dynamic viscosity, respectively.

Bakshi *et al.*[11] studied the impact of droplets on a sphere from a side view. Using this approach, the lamella was "lifted" upward in order to have a free lateral view and, therefore, the possibility for the measurement. The obtained results were later used for deriving an analytical model predicting the temporal development of the lamella thickness.[8,12]

A very well-known method for measuring thin liquid films is Confocal Chromatic Interference (CCI), which is well described in the literature.[13] CCI is a point measurement method analyzing color shifts due to chromatic aberration and interference. The design for the experimental setup using this method for measuring the lamella thickness at the droplet impact point seems to be very challenging since the sensor should be located perpendicular to the surface. Therefore, the sensor head is located inside the trajectory of the falling droplet, which makes an impacting droplet onto the film impossible. Furthermore, it should be noted that a minimum intensity is required for the reflections to be analyzed, which leads to the fact that the difference in the refractive indices Δn at the interfaces must be higher than a certain minimum.

Lagubeau *et al.*[10] used the computer-based space-time-resolved Fourier Transform Profilometry (FTP), which measures the shape of 3D objects with the help of a fringe pattern.[14,15] This enabled a tracking of the droplet shape evolution during the impact, including the lamella thickness. The deformation of the pattern projected into the droplet impact area resulting from the changing height and shape of the liquid–air interface is recorded using a fast camera. When comparing the fringe pattern on the droplet and on a flat reference surface, software can be used to determine the different thicknesses.

To the authors' knowledge, there have been only a few measurements of the lamella thickness and, especially, no broad parameter study investigating the influence of surface wettability on the lamella thickness. Therefore, the rather newly proposed measurement technique reported by Foltyn *et al.*,[4] the LASER Pattern Shift Method (LPSM), is used in a slightly altered approach using naturally occurring patterns, i.e., the bubble shadows observable during each droplet impact onto smooth walls. Compared to the CCI, this method has the advantage that it is based on transmission and can therefore be used with small differences in refractive indices Δn.[4] Furthermore, there is no conflict between the sensor and the falling droplet when measuring the lamella thickness during the droplet impact since the observation is done from below. In comparison to FTP, the LPSM has a simpler setup since it works with naturally occurring patterns and no additional pattern needs to be projected into the test section. In addition, the calculation of the lamella thickness using the LPSM is significantly less complex because the formula only needs to be derived once and can then be used instantly.

TABLE I. Summary of the evaluated parameters. For each parameter, the indicated range of values is given. The experiments that require a plasma treatment to modify the wetting behavior are marked by superscript *.

Liquid		Distilled water				Isopropanol (2-propanol)			
Material		PMMA		PC		PMMA		PC	
Contact angle		0°*		0°*		0°		0°	
		25°–40°*		25°–40°*					
		75.1°		79.8°		66°–73°*		66°–73°*	
		117°–122°*		117°–122°*					
Plasma treatments		Plasma activation (*) and plasma polymerization (*)							
Impact conditions	Re:	4130	6860	9360	12 240	1135	1745	2315	2955
	We:	80	205	385	665	165	400	715	1165
Surface structure		Smooth							

Almost all parameters are known in advance just by the geometric arrangement of the experimental setup, except one parameter that is measured.

The present paper shows that the LPSM is a powerful film thickness measurement technique. Several impact experiments with different parameters (cf. Table I) were investigated with the focus on their influence on the lamella thickness and the dependency between the minimum lamella thickness and the Reynolds number. The variation of the used liquid and the impact velocity resulted in different Reynolds and Weber numbers ($We = \rho D u^2/\sigma$, where σ is the liquid surface tension) in the ranges of $1135 < \mathrm{Re} < 12\,240$ and $80 < We < 1165$, respectively.

The obtained results helped to prove the validity of the analytical solution of Roisman[8] and Roisman *et al.*[12] for full wetting isopropanol droplets. However, it could also be shown that the actual correlations are not taking different wettabilities and viscosities into account so that some insights into possible modifications are suggested.

II. PHYSICAL BACKGROUND

A. LASER Pattern Shift Method (LPSM)

If a LASER beam is directed at a prism as shown in Fig. 1, it is deflected at the interface between the prism and ambient air due to their different refractive indices n_i (Fig. 1, beam path 1). A liquid film with the height h_F on the prism causes a displacement of the LASER beam by the length d_{Cam} (Fig. 1, beam path 2). This phenomenon is the basis of the measuring method according to Foltyn *et al.*[4]

Various trigonometric correlations and Snell's law of refraction, as given in Eq. (1), are used to derive the analytical relationship between the two quantities d_{Cam} and h_F,[16,17]

$$n_{In} \sin \xi_{In} = n_{Out} \sin \xi_{Out}, \tag{1}$$

where ξ_{In} is the angle of incidence, ξ_{Out} is the angle of refraction with respect to the normal, n_{In} is the refractive index of the medium on the entrance side, and n_{Out} is the refractive index of the medium on the exit side. For the total reflection case, Snell's law from Eq. (1) can be written as follows using the total reflection angle ξ_t:

$$\xi_t = \arcsin\left(\frac{n_{Out}}{n_{In}}\right). \tag{2}$$

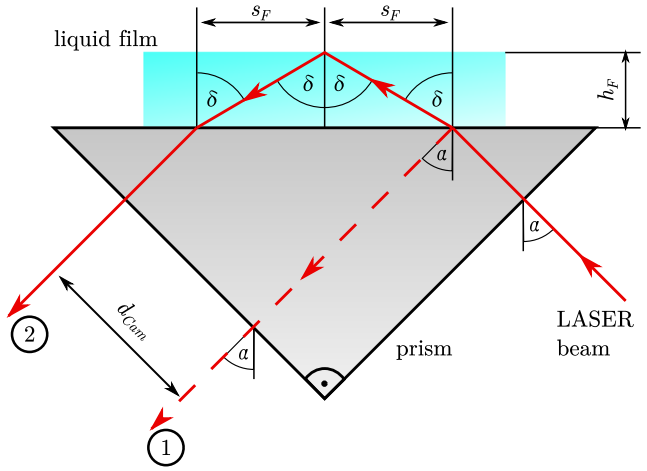

FIG. 1. Path of a LASER beam through a prism without (path 1) and with (path 2) a liquid film. Adapted with permission from Foltyn *et al.*, 29th Conference on Liquid Atomization and Spray Systems, Paris, France, 2–4 September 2019, ilass19.sciencesconf.org/24623. Copyright 2019 ILASS–Europe.

With the two introduced equations, the course of the LASER beam shown in Fig. 1 can be now described. In this figure, α and δ correspond to ξ_{In} and ξ_{Out} from Eq. (1), respectively. Due to the experimental setup, the angle α in our case is 45°. Therefore, the angle of incidence for the entering LASER beam is $\alpha + 45° = 90°$, and the beam is not deflected further at the transition into the prism. At the interface between the prism and the liquid film, the beam has an angle of incidence of $\alpha = 45°$. With the help of Snell's law from Eq. (1), the exit angle δ inside the liquid film can be determined as follows:

$$\delta = \arcsin\left(\sin(\alpha)\left(\frac{n_P}{n_F}\right)\right). \tag{3}$$

Here, n_P corresponds to the refractive index of the prism, while n_F corresponds to that of the liquid. The exact values can be taken from Table II. The angle δ does not change during the ray path within the liquid due to the inter-angle relationship and the total reflection at the interface between the liquid and surrounding air (see Fig. 1, path 2). In the further course of the LASER beam, it hits the interface between the liquid and prism a second time and passes through the prism with the angle α as before.

In comparison to the dry case in Fig. 1 (path 1), a horizontal displacement s_F of the LASER beam occurs due to the liquid film, which leads to the displacement d_{Cam}. In the following, the most important steps of the derivation to calculate the height of the liquid film h_F with a horizontal alignment according to Foltyn *et al.*[4] are summarized.

The displacement s_F can be described with the help of the displacement d_{Cam} or by the height of the liquid film h_F as follows:

$$s_F = \frac{d_{Cam}}{2\cos(\alpha)}, \tag{4}$$

$$s_F = h_F \tan(\delta). \tag{5}$$

Equating Eqs. (4) and (5) results in

$$\frac{d_{Cam}}{2\cos(\alpha)} = h_F \tan(\delta). \tag{6}$$

TABLE II. Thermophysical properties of distilled water and isopropanol (2-propanol) at 25 °C and refractive indices n of the liquids and the prism at a wavelength of 680 nm.

	Distilled water	Isopropanol (2-propanol)	Unit	References
Dyn. viscosity μ	0.8897	2.045	(mPa s)	34,35
Surface tension σ	0.071 98	0.020 92	(N m^{-1})	36,37
Density ρ	997.1	781.5	(kg m^{-3})	38,39
Refractive index n_F	1.3310	1.3746	···	40,41
	Glass NBK-7			
Refractive index n_P	1.5136		···	42

The searched value h_F is now directly related to the measured size d_{Cam}. If δ in Eq. (6) is replaced by Eq. (3), it follows

$$\frac{d_{Cam}}{2\cos(\alpha)} = h_F \tan\left(\arcsin\left(\sin(\alpha)\left(\frac{n_P}{n_F}\right)\right)\right). \tag{7}$$

With the help of the trigonometric relation $\tan(\arcsin(x)) = \frac{x}{\sqrt{1-x^2}}$, given in the literature,[17] it follows

$$\frac{d_{Cam}}{2\cos(\alpha)} = h_F \frac{n_P}{n_F} \sin(\alpha) \frac{1}{\sqrt{1-\sin(\alpha)^2\left(\frac{n_P}{n_F}\right)^2}}. \tag{8}$$

Rearranging gives

$$h_F = \frac{1}{2} d_{Cam} \frac{n_F}{n_P} \sqrt{1-\sin(\alpha)^2\left(\frac{n_P}{n_F}\right)^2} \frac{1}{\sin(\alpha)\cos(\alpha)}. \tag{9}$$

Finally, under the assumption of a horizontal fluid surface, Eq. (9) can be used to calculate the height h_F as a function of the displacement d_{Cam}. Since only the top layer of a multi-layer compound is measured, the addition of the plane-parallel polymer specimen only causes the beams to be shifted parallel.[4] Therefore, it has no influence on the measurement result. The refractive indices n_F and n_P and the angle α are determined by the experimental setup and are known in advance.

For the special case of application to determine the lamella thickness h_F at the droplet impact onto a smooth solid surface, an air bubble that is entrapped at the impact point is the key element.[18–22] The formation mechanism of this air bubble is defined in detail in Sec. II D. From this air bubble, two shadows are generated in the bottom view due to the thickness of the liquid film lamella, and they are used as an indication of the required pattern shift. These shadows are shown magnified in Fig. 2. The change in the lamella thickness causes the distance between the two shadows d_S to change as well. Therefore, Eq. (9) can be adapted and simplified considering $\alpha = 45°$ as follows:

$$h_F = d_S \frac{n_F}{n_P} \sqrt{1-\frac{1}{2}\left(\frac{n_P}{n_F}\right)^2}. \tag{10}$$

B. Bubble entrapment

Based on the study by Rioboo *et al.*,[23] the droplet impact can be generally divided into four phases [see Fig. 3(a)]. The first phase is the kinematic phase. The droplet flattens after having impacted onto the surface and resembles a cut sphere. The upper part of the droplet remains unchanged at first and continues to approach the wall. The diameter of the contact area on the smooth surface increases continuously. In the second phase, the spreading phase, a thin film forms from the center of the droplet (lamella) with increasing time, which is bordered by a raised edge (rim). In the relaxation phase (phase 3), the lamella decelerates strongly and reaches a constant diameter. Furthermore, capillary waves are formed at the rim of the droplet and travel to its center. In the last phase (phase 4), the droplet contracts strongly, or for highly wettable surfaces, it continues to slowly wet the surface. The experiments performed by Rioboo *et al.*[24] showed that for low-wetting surfaces, a rebound of the droplet takes place. In this case, only a part or the whole droplet is detached from a jet. This is due to the surface tension, which causes the droplet to contract after the relaxation phase and forms a jet.

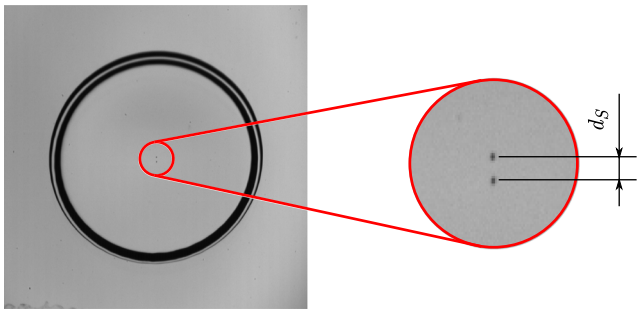

FIG. 2. Two bubble shadows of the entrapped air in the droplet with the distance d_S between the shadows.

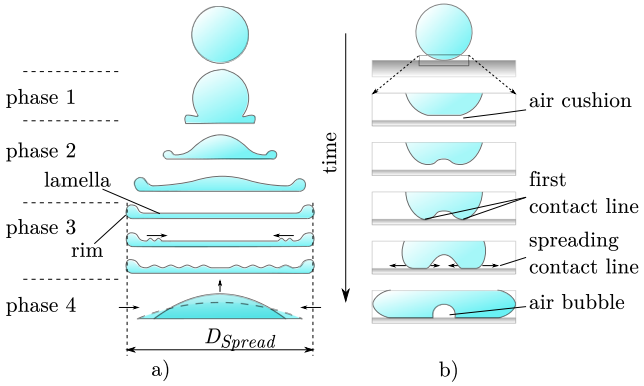

FIG. 3. Schematic representation of the phases during the droplet impact and illustration of the bubble entrapment: (a) during the impact, the rim and the lamella of the droplet are formed and capillary waves travel from the rim to the center and (b) interaction of the droplet with the impact surface, while the displaced air is trapped in the droplet as a bubble. Adapted with permission from Visser *et al.*, Soft Matter **11**, 1708 (2015). Copyright 2015 Author(s), licensed under a Creative Commons Attribution (CC BY) license.

As shown in Fig. 3(b), during the initial phase of the droplet impact, air is trapped at the interface between the solid surface and the spreading droplet. Experimental investigations by van Dam and Le Clerc[18] showed that the forming bubble can be located in the center of the droplet. Early investigations by Chandra and Avedisian[2] attributed this phenomenon to the air cushion formed between the droplet and the wall shortly before the impact. This was also shown by the numerical simulations performed by Mehdi-Nejad *et al.*[25] Continuous sinking causes a pressure buildup below the droplet, which leads to a depression of the droplet surface.[20–22,26] The air cushion initially prevents the contact between the droplet and the wall. As air continues to escape from the gap, an annular contact line between the droplet and the wall is created. From this contact line, the wall is wetted inward toward the center of the droplet and outward.[27] Therefore, the air is finally entrapped and forms a bubble inside the droplet.[2,18,25]

Figure 3(a) also shows the propagation of the capillary waves from the edge to the center of the droplet at the end of the spreading phase. Thoroddsen *et al.*[19] explained this phenomenon by the

decrease in spreading velocity when it reaches its maximum spreading diameter. Before the wave formation, the liquid of the droplet spreads outward faster than the waves can propagate on the lamella surface. Due to dissipation processes inside the droplet core (viscous effects) and the solid interface, as well as the transfer into surface energy, the spreading velocity decreases. One modeling approach has been suggested by Attané *et al.*,[28] although the relation of the respective energy portions depends on many influencing parameters. Within the third phase, the spreading velocity further decreases until the droplet spreading diameter has reached its maximum. Capillary waves can travel from the outer rim to the inner center of the droplet lamella as soon as their propagation velocity becomes larger than the local spreading velocity of the liquid sheet (see Fig. 4). The shown sample images are extracted from the later presented parameter study and are reduced to about a quarter of the image section for better illustration.

C. Experimental setup

The experimental setup for the lamella thickness evaluation is shown schematically in Fig. 5 and is one part of the multi-perspective droplet impact facility of Foltyn *et al.*[29] Therefore, only the relevant parts are described in this paper.

The droplet is generated using a precise syringe pump that is connected to a blunt needle with an outer diameter of 0.4 mm. A continuous droplet chain is generated at a flow rate of 0.5 ml min^{-1}. One random droplet of the droplet chain is selected manually to pass the droplet barrier and enters the test section. To control the droplet velocity, the height of the needle can be adapted. The droplet passes a light barrier, which triggers the *Photron SA-X2* high-speed camera, acquiring the images with a frame rate of 20 000 fps at a resolution of 1024 × 672 px^2 and a shutter speed of 1/88 888 s. The images are taken from the bottom perspective of the experiments performed by Foltyn *et al.*[29] using the total internal reflection at the upper surface of the transparent polymeric surface specimen. For this, the light of a LED and a lens is led through a glass diffuser plate entering the prism. To ensure that the light enters also the surface specimen, a thin isopropanol film is used as coupling media in between the upper prism surface and the surface specimen. After the total internal reflection at the upper surface of the specimen, the light leaves the prism and enters the *Navitar 12X System* far-field

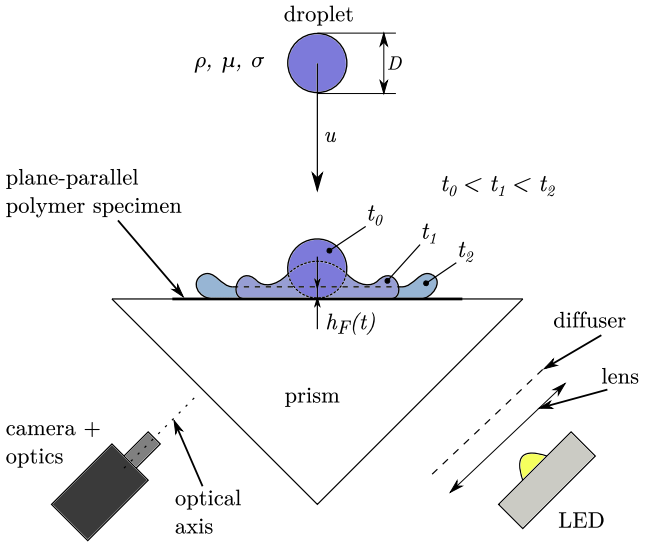

FIG. 5. Schematic representation of the experimental setup. Here, D denotes the droplet diameter, u the velocity, and $h_F(t)$ the time-dependent lamella thickness. The liquid properties are represented by ρ, μ, and σ for density, dynamic viscosity, and surface tension, respectively.

microscope and the high-speed camera (see the principle sketch in Figs. 1 and 5).

Wetted surfaces that do not fulfill the conditions of the total internal reflection of Eq. (2) are detected as dark spots on the camera chip. The usage of the glass diffuser plate can, however, generate a more distinct pattern instead of just dark and bright (see Fig. 6). This is because a single grit of the glass diffuser plate can be seen as one single point source at which the light is scattered. The intensity of the scattered light decreases with increasing deviation to the optical axis of the ray bundle due to the scattering characteristics. As a consequence, the acquired images have many different shades of gray values. The very bright values correspond to areas that completely fulfill the total internal reflection condition of Eq. (2). With increasing local surface tilt, no matter to which direction in regard to the optical axis, fewer (scattered) light rays reach the camera chip. Consequently, the lower the local pixel values, the

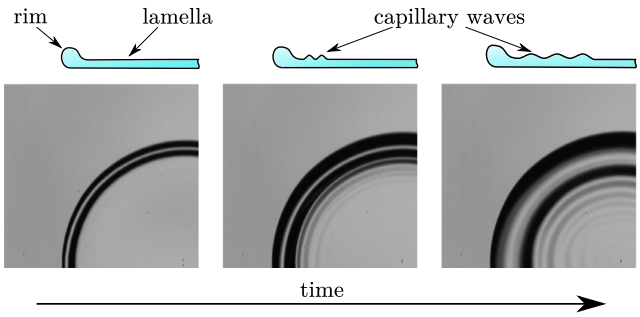

FIG. 4. Capillary waves spreading from the edge to the center of the droplet in time from left to right. Sample images are reduced to about a quarter of the image section for better illustration. Above the pictures, the respective sketches of the droplet cross section can be seen.

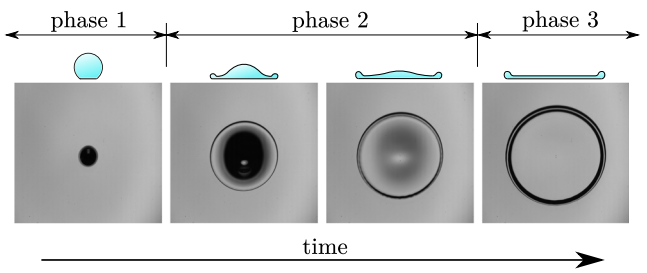

FIG. 6. Horizontal alignment of the droplet surface over time from left to right in phases 1 to 3 of Fig. 3. Due to the diffuse light, a bright inner surface of the droplet means a horizontal alignment of the surface. Above the pictures, the respective sketches of the droplet cross section can be seen.

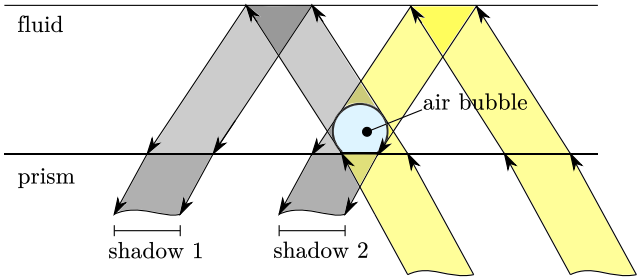

FIG. 7. Schematic representation of the formation of the two bubble shadows caused by the blocking of different light bundles due to the entrapped air bubble.

higher the angle between the local liquid surface and the horizontal prism surface. One can interpret this as an optical derivation of the surface profile. With the help of these properties, the time range during which the surface can be considered as horizontal is definable (see Sec. III C). During the time of a horizontal lamella, the LPSM method is then applied for calculating the lamella height h_F using Eq. (10).

D. Formation of the two bubble shadows

The formation of the two bubble shadows is shown schematically in Fig. 7. Both shadows are due to the total internal reflection occurring at the liquid surface and the blocking of different light bundles by the entrapped air bubble. The light bundle that hits the air bubble directly after the interface between the prism and liquid results in shadow 1. Shadow 2 is created by a light bundle that passes through the liquid and hits the bubble after the total internal reflection. Due to the described process of the droplet impact in Sec. II B, the air bubble can always be localized in the center of the droplet impact area. It does not change the position at all since it sticks to the surface, and no visual movement could be detected in the experiments. The reason for this behavior is that in the described impact phases 1 to 3 (see Fig. 3), an impingement flow occurs as a result of the impact.[30–32] This results approximately in a potential flow due to which the liquid flows from the center of the droplet outward. In order to change its position, the air bubble would need to loosen itself from the surface it is sticking to and rise inside the liquid sheet. This event is very unlikely due to the symmetric flow conditions and the adhesion forces of the bubble. This was only observed in one single case in more than 550 of our experiments. Consequently, shadow 2 in Fig. 7 is always at the same position, while shadow 1 changes its position with the height h_F of the droplet lamella. The lower the height, the smaller the distance between shadows 1 and 2. In reverse, as mentioned before, the distance between the bubble shadows can be used to determine the height of the lamella using Eq. (10).

III. EXPERIMENTAL APPROACH

A. Parameter space

The used parameter space for the presented studies corresponds to that in the study by Foltyn *et al.*[29] and is summarized in Table I. The droplet impact experiments have been conducted using two droplet liquids, either distilled water or isopropanol (2-propanol). The respective fluid properties at 25 °C are listed in Table II. The droplet impacted onto smooth transparent surfaces made of Lexan® (Polycarbonate, PC) or Plexiglas® [Poly(methyl methacrylate), PMMA]. The wetting behavior of the polymer specimens has been modified by plasma activation and plasma polymerization and characterized by the sessile drop method measuring the apparent contact angle θ. This apparent contact angle does not need to be the Young contact angle θ_Y known from the literature.[33] However, the found apparent contact angle gives enough information in order to characterize the wetting behavior of the solid–liquid system appropriately. For further information, the reader is referred to the literature.[29] In total, four different wetting behaviors for water and two different wetting behaviors for isopropanol could be achieved (see Table I). The respective contact angles are used then for further evaluation. Moreover, four different impact velocities have been chosen, resulting in the provided pairs of Re and *We* numbers for the respective droplet fluid.

B. Experimental procedure

The experimental procedure is described also in the study by Foltyn *et al.*[29] and summarized as follows: Every single experiment has been repeated at least ten times. The set of ten experiments at constant impact parameters is considered as one experimental set. Before the polymer specimens could be used, the desired wetting behavior had to be established for the experimental set according to the methods given in Table I. After the treatment, the reference contact angle has been measured by the sessile drop method on additional spare specimens, which have been treated together with the used specimens to maintain data consistency. However, the plasma treatments were applied separately for each set of impact parameters, providing a reference range of contact angles.[29] These contact angles were then also used later for further evaluations.

In order to conduct the droplet impact experiments, the samples had been brushed, at first, with a *PFA Nitrogen Gun* by *Parker Hannifin Corporation* using high purity nitrogen (99.999%) to carry away all dust particles. Afterward, the thin isopropanol coupling media was applied on the prism, and the polymer specimen was placed then on top of the film. In addition to the coupling of light into the polymer specimen, the adhesion forces were keeping the sample at its place. Then, the droplet stream was started, and after the establishment of a continuous droplet chain with constant droplet sizes and falling trajectory, one random droplet was selected to pass the droplet barrier falling into the test section. The droplet impacted onto the surface that was recorded using the triggered camera.

C. Evaluation routine

For the evaluation of the respective impact experiments, a MATLAB® routine was developed, which automatically determines the searched lamella thickness h_F in the area of a horizontal surface. In general, the procedure of the evaluation routine can be described as follows: After the raw images have been imported, they are vertically resized to compensate the distortion caused by the experimental setup. Then, the droplet impact frame is determined. For this purpose, the background of the images is removed and then globally binarized using Otsu's method.[43] As a result, only the wetted droplet

area can be seen on the binary frames. Consequently, as long as the droplet does not touch the surface, there are no areas to be seen in the images. In the event of the droplet impact, the number of tracked binary areas increases by one. Therefore, the instant of the droplet impact can be determined as the frame when the number of areas is incremented by one. Afterward, the temporal range of a horizontal aligned droplet lamella surface is searched in order to apply Eq. (10) with the frames after the impact. For this purpose, start and end criteria were developed, which determine the start and end frames of the evaluation range. The criteria are based on the different gray values of the pixels within the droplet since these provide conclusions about the orientation of the surface (see Sec. II C). The start criterion detects the first occurrence of the horizontal surface via the mean value and the standard deviation of the pixel values. If a certain brightness (consideration of the mean values) and a presented homogeneous distribution (consideration of the standard deviation) are reached, it can be assumed that a horizontal surface is given. The end criterion then uses the gray values to check from which point onward, due to the capillary waves running toward the center and appearing darker, these both conditions are no longer fulfilled, and thus, a horizontal surface no longer exists.

In order to obtain the time-dependent lamella thickness $h_F(t)$, the distance between the centroids of the bubble shadows d_S is evaluated over time, and Eq. (10) is applied. Since the bubble shadows move toward each other as the lamella thickness decreases, it may happen that the individual shadows are no longer recognizable as such but as an overall surface. In this case, a specially developed routine reconstructs the current shadow areas with the help of previous reference areas to be able to obtain data also for touching shadows.

D. Processing of results and uncertainty analysis

As described in Sec. III B, each experiment was repeated minimum ten times with the parameters listed in Table I. Using the evaluation routine described above (Sec. III C), the thickness of the lamella is calculated over time for each experiment. Here, an almost exponential behavior of the lamella thickness can be seen. For this reason, the individual courses are fitted with the Curve Fitting Toolbox™ of MATLAB® and Eq. (11) using the trust-region algorithm and bisquare weighting,

$$h_F(t) = a\,\exp(bt) + c. \tag{11}$$

Here, $h_F(t)$ corresponds to the fitted lamella thickness value and t to the measured time from the impact frame. The coefficients a, b, and c are used to fit the curve to the original values and are determined for each experiment. In order to compare the experiments of identical parameters with others, the curves are summarized to one dataset each using arithmetical mean values. Here, a standard deviation of the lamella thickness h_F of about ±5% for isopropanol and about ±4% for distilled water could be determined. Due to the resolution accuracy of the camera with a pixel size of 20 μm,[44] an error of $\Delta h_F = \pm 1$ px occurs, which corresponds approximately to $\Delta h_F = \pm 17$ μm. Since only pure substances had been used, it can be assumed that there is no significant influence of the liquid properties onto the optical system and the results. Therefore, the accuracy of the measurement technique is governed by the resolution and can be significantly enhanced by using a camera with a smaller pixel size.

IV. RESULTS

A. Dimensional results

In the following, the respective effects of the experimental parameters on the lamella thickness are presented. For this purpose, selected data are depicted in Fig. 8.

The influence of the used liquids is due to their different viscosities and surface tensions. With an approximately two times greater viscosity than water (cf. Table II), isopropanol is more viscous and spreads more slowly on the prism. For this reason, the lamella thickness decreases slower in comparison to water [see Fig. 8(a)]. Moreover, since the surface tension of isopropanol is only about a third of that of water (cf. Table II), the droplet contracts later, causing the horizontal surface to appear longer [cf. Fig. 8(a)]. With regard to the liquid property relations, it was observed that the minimum lamella thickness for isopropanol is about twice that of water. Additionally, the temporal range of a horizontal droplet surface is about one and a half times larger for isopropanol than for water. In general, it can be said that the lower the viscosity of the liquid, the faster the lamella thickness decreases, and the greater the surface tension, the smaller the temporal evaluation range, which is equal to the shorter time of a horizontal surface (see phase 3 of Figs. 3 and 6).

The different impact velocities were realized by using different droplet falling heights. In this case, the lamella thickness decreases with the increasing falling height and the evaluation range becomes larger [see Fig. 8(b)]. This is due to the fact that a droplet with higher velocity spreads wider on the surface and the lamella must become thinner due to the conservation of mass. Furthermore, with a larger maximum spreading diameter, it takes longer for the capillary waves to reach the center of the droplet lamella, resulting in a longer temporal evaluation of the film thickness.

The wetting behavior was analyzed on the basis of different contact angles. It was observed that as the contact angle increases, the lamella becomes thicker and the evaluation range decreases [see Fig. 8(c)]. This can be explained as follows: If the contact angle is smaller, the droplet spreads wider on the polymer specimen than with large contact angles. At the same time, it reaches a larger maximum spreading diameter, and due to the conservation of mass, the lamella becomes thinner. As explained before, a larger maximum spreading diameter also results in a larger evaluation range.

It was observed that when using the different polymer specimens, PC and PMMA, the curves of the lamella thickness hardly differ from one another [see Fig. 8(d)]. It can also be seen that the values of the material under observation are within the error bars of the other material [cf. Fig. 8(d)]. This means that only a very minor or negligible influence on the lamella thickness could be detected for the material of the polymer specimen.

From the presented results, it can be summarized that the chosen liquid, the impact velocity, and the wetting behavior have a significant influence on the lamella thickness. The material of the used polymer specimen has only a minor influence. With the parameters from Table I, it could be seen that the lamella has a thickness ranging from $h_F = 50$ to 190 μm when isopropanol is used. If water is used,

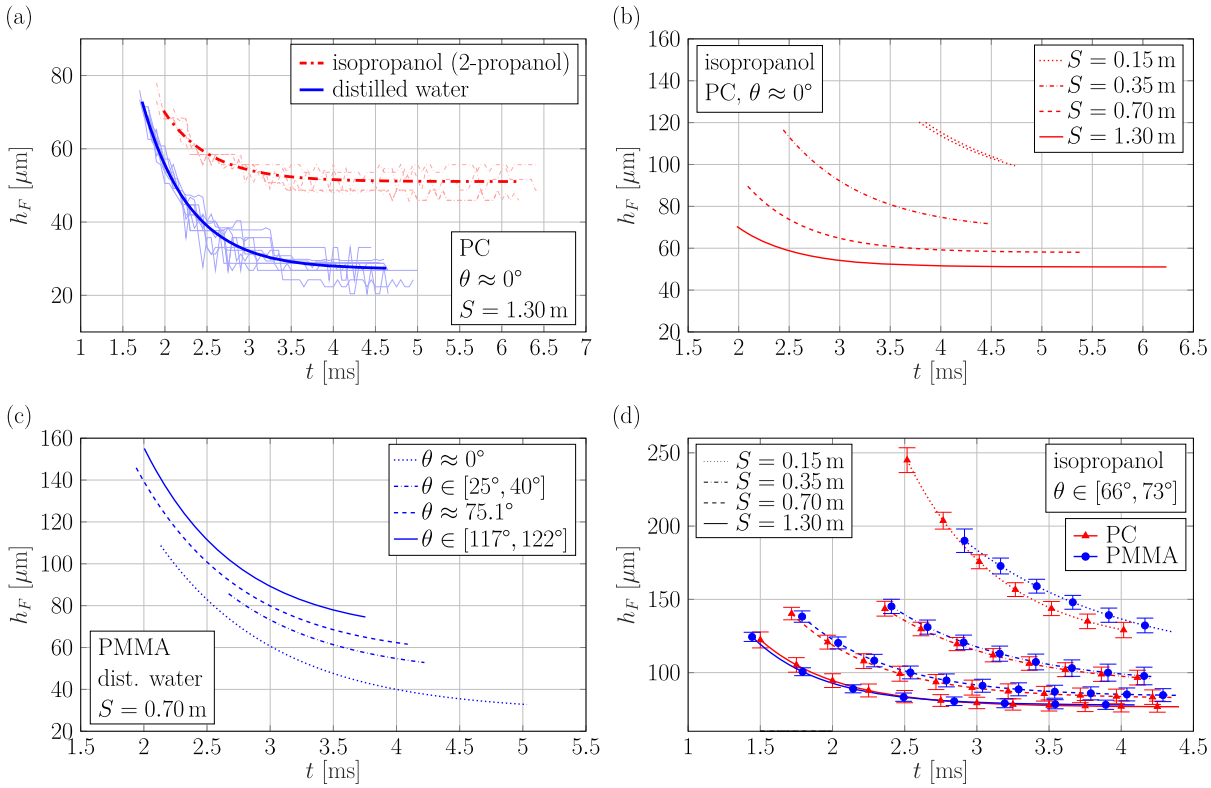

FIG. 8. Lamella thickness over time considering different influencing parameters. The parameter S corresponds to the falling height and θ to the measured apparent contact angle. In (a), the influence of the liquid on the droplet impact at $S = 1.30$ m and $\theta \approx 0°$ onto PC is shown. The actual data before the fitting are also displayed here. In (b), the influence of the impact velocity on the droplet impact with the variation of the falling height for isopropanol and PC at $\theta \approx 0°$ is depicted. In (c), the influence of the contact angle θ for distilled water droplets impacting onto PMMA for $S = 0.70$ m is shown. In (d), the influence of the polymer specimen material at different falling heights for the isopropanol droplet impact and $\theta \in [66°, 73°]$ is visualized. Here, error bars are included.

the range of the measured lamella thickness is between $h_F = 30$ and 170 μm.

B. Dimensionless results

In the following, the experimentally obtained results using the extended LPSM technique shall be compared to available analytical solutions. Since the LPSM measures the film thickness in the middle of the droplet lamella, only analytical solutions located at the symmetry axis are used.

Semi-empirical solutions for describing the dimensionless film thickness $\widetilde{h} = \frac{h_F}{D_{imp}}$ have been developed by several researchers. Yarin and Weiss[5] developed an expression for the temporal development of film thickness considering an inviscid flow,

$$\widetilde{h}_{inv} = \frac{\eta}{(\tau + \tau_0)^2}. \tag{12}$$

Here, $\tau = \frac{ut}{D}$ corresponds to the dimensionless time and η and τ_0 are the fitting parameters. Roisman and colleagues[8,12] continued the development by adding the viscous solution (13) to the existing solution of Yarin and Weiss.[5] This results in

$$\widetilde{h}_{visc} = \frac{4\gamma}{5}\frac{\sqrt{\tau}}{\sqrt{Re}}, \tag{13}$$

$$\widetilde{h} = \widetilde{h}_{inv} + \widetilde{h}_{visc}, \tag{14}$$

$$\widetilde{h} = \frac{\eta}{(\tau + \tau_0)^2} + \frac{4\gamma}{5}\frac{\sqrt{\tau}}{\sqrt{Re}}. \tag{15}$$

This allows the film thickness to be calculated using Eqs. (14) and (15). Using experimental data[11] and numerical simulations,[12,45–47] the fitting coefficients were estimated in the literature[8] as $\eta = 0.39$, $\gamma = 0.6$, and $\tau_0 = 0.25$. In the previously mentioned references, mainly alcohols and low surface tension liquids, i.e., isopropanol, were used, showing mostly a full wetting behavior. The available data had a range of $58 < \mathrm{Re} < 100\,000$ and $16 < We < 16\,000$. Therefore, this data range is sufficiently large to allow a comparison of the data obtained in this study with the derived correlations in the literature.

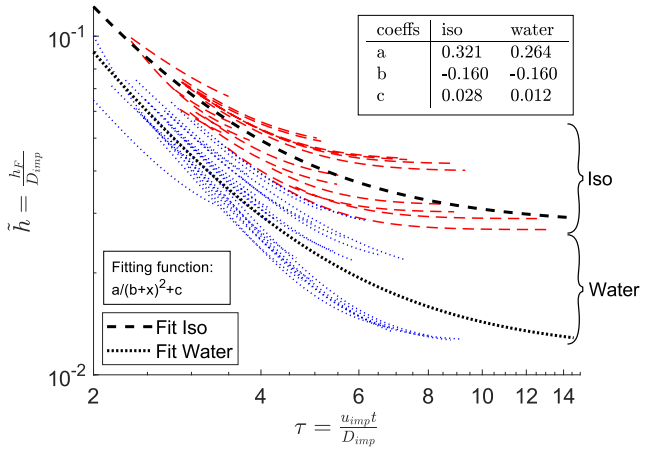

FIG. 9. Dimensionless film thickness over dimensionless time for all performed parameter sets. The fits are for the full set of the respective fluids and result in the provided coefficients.

The residual film thickness, which is the predicted minimal film thickness of the lamella, was derived by Roisman[8] as follows:

$$\widetilde{h}_{res} = 0.79\mathrm{Re}^{-2/5}. \tag{16}$$

The correlation of $\widetilde{h}_{res} \sim \mathrm{Re}^{-2/5}$ has also been established by other scientists.[7,9,10] With regard to the experimental results, the time for defining the minimal film thickness is more difficult to obtain than in the analytical solution. In the experiments, when the maximum spreading diameter is reached, capillary waves could be observed moving to the lamella center (see Fig. 4). This will then define the end of the measurement time frame and will also lead, obviously, to a non-horizontal lamella surface (cf. Sec. III C). Therefore, the last value of the lamella thickness measured by the LPSM within the time evaluation range was chosen as the experimental residual layer thickness. This procedure is motivated by two reasons: First, the definition of the approximate horizontal film holds for both cases, the analytical solution and the experiments. Second, a definition of a residual film thickness is only appropriate for horizontal liquid layers.

Figure 9 shows the dimensionless film thickness plotted over the dimensionless time for each parameter set. It can be clearly distinguished between the measurements of impacting distilled water droplets and impacting isopropanol droplets since the film thickness for isopropanol is always higher. The fitting was performed using a non-linear least-squares approach, the trust-region algorithm, and a bisquare weighting. The fitting equation $a/(b+x)^2 + c$ has been suggested by Lagubeau *et al.*[10] and has also the structure of Eq. (15). The coefficients a and b correspond in that case to η and τ_0 of Roisman,[8,12] respectively, while c can be considered as the viscous solution. The coefficient b had in the first fitting approach almost the same values. Therefore, the same value for both fits has been established to take also a unique τ_0 value in Eqs. (12) and (15) into account. What can be also easily seen in Fig. 9 is the wide spread of the different data lines. This behavior can be mainly explained by the different wetting behaviors (see Sec. IV A) with the dimensional results. This means that a uniform equation for the analytical description of the film thickness or for fitting the results into the provided representation does not appear to be suitable since the influence of different wetting behaviors is not taken into account.

Looking now at the two equations, (15) for predicting the temporal development of the film thickness in the center of the droplet lamella and Eq. (16) for predicting the residual film thickness, the following conclusions can be drawn. In the case of isopropanol with comparably low surface tension and a full-wetting behavior ($\theta \approx 0°$), the two correlations with the proposed coefficients fit very well [see Figs. 10(a) and 11]. The influence of the surface material seems to be negligible. However, increasing the apparent contact angle for isopropanol results in an increase in the residual film thickness. Therefore, both correlations do not fit that well anymore. For example, in Fig. 11, the line fitting the respective experimental data has the same

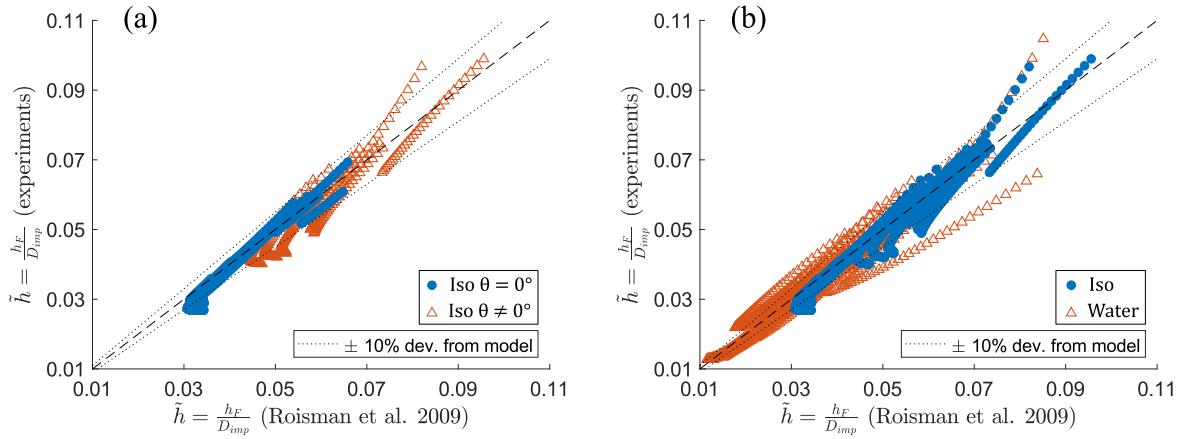

FIG. 10. Comparison of the experimentally obtained temporal development of lamella thickness using the LPSM with the analytical correlation of Roisman:[8] (a) only for isopropanol cases with different wetting behaviors and (b) comparison of isopropanol cases to water cases. For the analytical correlation used for distilled water, a modification of the parameter $\gamma = 0.3$ in Eq. (15) was necessary.

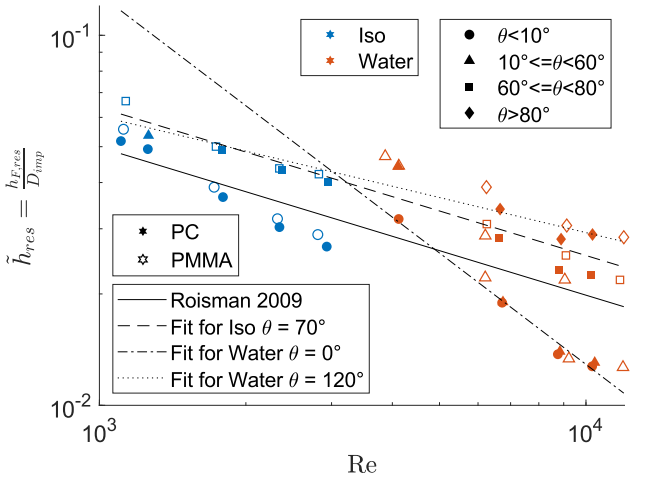

FIG. 11. Experimental residual film thickness in dependency of the Re number, wetting behavior, surface material, and droplet fluid, as well as the correlations of Roisman.[8] Using the structure of this correlation, further lines have been fitted, indicating the liquid and the wetting behavior.

exponent of −2/5 but a 1.28 times higher coefficient (1.28 × 0.79). For the experiments with water, it can be clearly determined that for some cases (mainly the full-wetting cases), the inviscid solution of Yarin and Weiss[5] is already almost sufficient for the prediction of the temporal film thickness development. The viscous effects in the model were in these cases always significantly too dominant. In order to limit this influence and also taking into account that the dynamic viscosity of water is approximately half of that of isopropanol, the factor γ for weighting this viscous solution for water was changed to $\gamma = 0.3$. This leads to a significant improvement of the fitting quality of the correlation vs the experimental results. However, also for the water cases, the increasing wetting behavior cannot be predicted by the modified correlation (15). Nevertheless, the deviations for the isopropanol and water cases, having an apparent contact angle of $\theta > 0°$, are now almost of similar magnitude. Since the contact angles of water have a much wider range, the deviations in comparison to the model of Roisman[8] are larger [see Fig. 10(b)]. Regarding the proposed correlation (16) predicting the residual film thickness (see Fig. 11), the water cases behave completely different as predicted. The influence of the surface material seems to be again negligible, but the influence of the Re number is stronger. Keeping the structure of the original correlation, the line for fitting the respective points for full wetting ($\theta \approx 0°$) can be described by $\widetilde{h} = 129\mathrm{Re}^{-1}$. Increasing the apparent contact angle θ will modify both fitting coefficients so that the equation for $\theta \in [117°; 122°]$ is defined as $\widetilde{h} = 0.533\mathrm{Re}^{-0.315}$.

A modification of Eq. (15) according to Eq. (17) could give very good results. However, using adjusting factors for this modification seems not to be physically consistent. Therefore, it might be better to provide a more physically motivated adjusted model,

$$\widetilde{h} = A(\theta, \mu, \ldots)\frac{\eta}{(\tau + \tau_0)^2} + B(\theta, \mu, \ldots)\frac{4\gamma}{5}\frac{\sqrt{\tau}}{\sqrt{Re}}. \qquad (17)$$

V. CONCLUSIONS

In this paper, it was demonstrated that the newly developed LPSM is very capable of measuring the lamella film thickness during droplet impacts on dry smooth surfaces. The liquid film thicknesses have been measured reliably in the original approach using a LASER as a pattern generating instrument.[4] By replacing this pattern with the naturally existing pattern, the two shadows of an air bubble that sticks to the solid surface, the lamella and film thickness are now able to be measured for droplet impacts onto dry surfaces and liquid films. Using the described image processing, the derived equations for the original LPSM can be simply reused for the new approach. However, it is important for the measurement application that a horizontal surface can always be guaranteed. A method to limit the evaluation time to the phase when a horizontal surface is expected has been presented.

The fact that the LPSM does not need further measurement equipment makes this technique very powerful and very attractive. All typical evaluations that can be done from the bottom or top perspectives observing the droplet impact can be performed. The application of the LPSM is then just an extension for gathering even more information on the experiments. The accuracy of the LPSM strongly depends on camera resolution, pixel size, and magnification. In the presented case, the film thickness could be determined with an uncertainty of ±17 μm. However, this can be significantly reduced by using a camera with a smaller pixel size. Several repetitions of the measurements also showed a significantly lower uncertainty in the experimental results. During the experiments, the typical film thickness range measured was between 30 and 190 μm.

To prove the capability of the new LPSM extension, droplet impacts using distilled water and isopropanol onto smooth dry polymeric surfaces with variable wetting behavior were investigated systematically. The wetting behavior was modified by plasma activation and plasma polymerization. The results showed that with increasing impact energy, the thickness of the droplet lamella decreases, while the time range in which a horizontal lamella surface can be found increases. Furthermore, it was observed that with increasing fluid viscosity, the total droplet lamella thickness increases and the duration at which the droplet lamella can be considered as horizontal decreases. The surface material has no influence on the lamella thickness since different materials with a similar wetting behavior result in the same outcome. However, the wetting behavior plays a significant role, and the lamella thickness increases with increasing contact angles. Analytical correlations predicting the film thickness have been compared to the experimentally obtained data. The proposed correlations for the temporal development of the film thickness and the residual film thickness seem to fit well for full wetting low-surface tension liquids. These were also mainly the liquids for which the fitting parameters were found. For liquids such as distilled water and higher apparent contact angles, the literature correlations do not fit well. The influence of the apparent contact angle on the dynamics in the boundary flow inside the droplet lamella seems to be more dominant. Therefore, further investigations should be done for predicting consistently the influence of different wetting behaviors and finding a physically motivated improved correlation.

ACKNOWLEDGMENTS

The authors acknowledge the financial support of this work from the Deutsche Forschungsgemeinschaft (DFG) in the frame of the International Research Training Group "Droplet Interaction Technologies" (*GRK 2160: DROPIT*) under Project No. 270852890. Additionally, the authors acknowledge the support of Fundação para a Ciência e a Tecnologia (FCT) through Ph.D. Scholarship No. SFRH/BD/140009/2018 and Project No. UIDB/50022/2020. Furthermore, the authors would like to thank Johannes Müller (ITLR) for the very fruitful discussions about occurring optical phenomena during the development of the extended LPSM.

AUTHOR DECLARATIONS

Conflict of Interest

The authors have no conflicts to disclose.

DATA AVAILABILITY

The data that support the findings of this study are available from the corresponding author upon reasonable request.

REFERENCES

[1] A. L. Yarin, Annu. Rev. Fluid Mech. **38**, 159 (2006).
[2] S. Chandra and C. T. Avedisian, Proc. R. Soc. London, Ser. A **432**, 13 (1991).
[3] M. Marengo, C. Antonini, I. V. Roisman, and C. Tropea, Curr. Opin. Colloid Interface Sci. **16**, 292 (2011).
[4] P. Foltyn, N. Roth, and B. Weigand, in 29th European Conference on Liquid Atomization and Spray Systems, Paris, France, 2–4 September 2019, ilass19.sciencesconf.org/24623.
[5] A. L. Yarin and D. A. Weiss, J. Fluid Mech. **283**, 141–173 (1995).
[6] C. Josserand and S. T. Thoroddsen, Annu. Rev. Fluid Mech. **48**, 365 (2016).
[7] A. I. Fedorchenko, A.-B. Wang, and Y.-H. Wang, Phys. Fluids **17**, 093104 (2005).
[8] I. V. Roisman, Phys. Fluids **21**, 052104 (2009).
[9] J. Eggers, M. A. Fontelos, C. Josserand, and S. Zaleski, Phys. Fluids **22**, 062101 (2010).
[10] G. Lagubeau, M. A. Fontelos, C. Josserand, A. Maurel, V. Pagneux, and P. Petitjeans, J. Fluid Mech. **713**, 50 (2012).
[11] S. Bakshi, I. V. Roisman, and C. Tropea, Phys. Fluids **19**, 032102 (2007).
[12] I. V. Roisman, E. Berberović, and C. Tropea, Phys. Fluids **21**, 052103 (2009).
[13] V. V. Lel, A. Kellermann, G. Dietze, R. Kneer, and A. N. Pavlenko, Exp. Fluids **44**, 341 (2008).
[14] M. Takeda and K. Mutoh, Appl. Opt. **22**, 3977 (1983).
[15] A. Maurel, P. Cobelli, V. Pagneux, and P. Petitjeans, Appl. Opt. **48**, 380 (2009).
[16] *Optik*, 3rd ed., edited by E. V. Hecht (Addison-Wesley, Bonn, 1994), p. 717.
[17] *Repetitorium der Höheren Mathematik*, 6th ed., edited by G. V. Merziger and T. V. Wirth (Binomi Verlag, 2010), p. 576.
[18] D. B. van Dam and C. Le Clerc, Phys. Fluids **16**, 3403 (2004).
[19] S. T. Thoroddsen, T. G. Etoh, K. Takehara, N. Ootsuka, and Y. Hatsuki, J. Fluid Mech. **545**, 203 (2005).
[20] M. M. Driscoll and S. R. Nagel, Phys. Rev. Lett. **107**, 154502 (2011).
[21] J. M. Kolinski, S. M. Rubinstein, M. Mandre, M. P. Brenner, D. A. Weitz, and L. Mahadevan, Phys. Rev. Lett. **108**, 074503 (2012).
[22] S. Mandre and M. P. Brenner, J. Fluid Mech. **690**, 148 (2011).
[23] R. Rioboo, M. Marengo, and C. Tropea, Exp. Fluids **33**, 112 (2002).
[24] R. Rioboo, C. Tropea, and M. Marengo, Atomization Sprays **11**, 12 (2001).
[25] V. Mehdi-Nejad, J. Mostaghimi, and S. Chandra, Phys. Fluids **15**, 173 (2003).
[26] S. G. Yiantsios and R. H. Davis, J. Fluid Mech. **217**, 547 (1990).
[27] C. W. Visser, P. E. Frommhold, S. Wildeman, R. Mettin, D. Lohse, and C. Sun, Soft Matter **11**, 1708 (2015).
[28] P. Attané, F. Girard, and V. Morin, Phys. Fluids **19**, 012101 (2007).
[29] P. Foltyn, D. Ribeiro, A. Silva, G. Lamanna, and B. Weigand, Phys. Fluids **33**, 063305 (2021).
[30] Y. Guo, Y. Lian, and M. Sussman, Phys. Fluids **28**, 073303 (2016).
[31] S. S. Kumar, A. Karn, R. E. A. Arndt, and J. Hong, Exp. Fluids **58**, 12 (2017).
[32] J. Philippi, P.-Y. Lagrée, and A. Antkowiak, J. Fluid Mech. **795**, 96 (2016).
[33] T. Young, Philos. Trans. R. Soc. London **95**, 65 (1805).
[34] M. L. Huber, R. A. Perkins, A. Laesecke, D. G. Friend, J. V. Sengers, M. J. Assael, I. N. Metaxa, E. Vogel, R. Mareš, and K. Miyagawa, J. Phys. Chem. Ref. Data **38**, 101 (2009).
[35] J. R. Rumble, *CRC Handbook of Chemistry and Physics, Viscosity of Liquids as a Function of Temperature* (CRC Press, Taylor & Francis Group, 2019).
[36] IAPWS, "Revised release on surface tension of ordinary water substance," Report No. R1-76 (International Association for the Properties of Water and Steam, 2014).
[37] J. R. Rumble, *CRC Handbook of Chemistry and Physics, Surface Tension at Various Temperatures* (CRC Press, Taylor & Francis Group, 2019).
[38] W. Wagner and A. Pruß, J. Phys. Chem. Ref. Data **31**, 387 (2002).
[39] J. R. Rumble, *CRC Handbook of Chemistry and Physics, Density Rho at the Temperature in °C Indicated by Superscript* (CRC Press, Taylor & Francis Group, 2019).
[40] G. M. Hale and M. R. Querry, Appl. Opt. **12**, 555 (1973).
[41] E. Sani and A. Dell'Oro, Opt. Mater. **60**, 137 (2016).
[42] Schott AG, "Optical Glass – Data Sheets," Report (2017), available at https://www.schott.com/d/advanced_optics/ac85c64c-60a0-4113-a9df-23ee1be20428/1.17/schott-optical-glass-collection-datasheets-english-may-2019.pdf.
[43] N. Otsu, IEEE Trans. Syst. Man Cybern. **9**, 62 (1979).
[44] *Photron Limited, Fastcam SA-X2 - Hardware Manual, 215F* (Photron Ltd., Chiyoda-Ku, Tokyo, 2018), rev 1.12 e ed.
[45] Š. Šikalo, H.-D. Wilhelm, I. V. Roisman, S. Jakirlić, and C. Tropea, Phys. Fluids **17**, 062103 (2005).
[46] J. Fukai, Y. Shiiba, T. Yamamoto, O. Miyatake, D. Poulikakos, C. M. Megaridis, and Z. Zhao, Phys. Fluids **7**, 236 (1995).
[47] S. Mukherjee and J. Abraham, J. Colloid Interface Sci. **312**, 341 (2007).